A predictive phase-field approach for cover cracking in corroded concrete elements

Available online at www.sciencedirect.com

ScienceDirect

Theoretical and Applied Fracture Mechanics 00 (202) 000–000

www.elsevier.com/

VSI: Fracture in concrete

A predictive phase-field approach for cover cracking in corroded concrete elements

Freddi Francesco[a]*, Mingazzi Lorenzo[a]

Departmend of Engineering and Architecture,
Università degli Studi di Parma,
Parco Area delle Scienze 181/A, Parma, 43124, Italy

Abstract

Steel bar corrosion is a crucial problem in reinforced concrete structures. Corrosion, being one of the most prevalent deterioration mechanism in concrete elements, has a significant impact on the structure's serviceability and durability, since the cross section of the steel reinforcement is reduced and the mechanical steel performances deteriorate. Additionally, residual material is created as a result of the steel oxidation process, and the volume occupied by the reinforcement grows, forcing the concrete cover to crack and spall. The carbonation-induced rebar corrosion and the subsequent cover cracking are simulated via the usage of a predictive model which combines the concrete carbonation process with the phase-field technique for brittle fractures. First, the carbon dioxide transport within the concrete is described using the Fick's second diffusion law. Then, the corrosion process is estimated via the electrochemical kinetics equations providing the associated steel expansion. The steel deformation and strain are calculated with the Faraday Law. Finally, a phase field approach for brittle material is used to reproduce rupture in the concrete cover. The developed model is validated against examples available in literature and representative examples are illustrated, describing the capability of the proposed approach to replicate the cover cracking in concrete.

Keywords: reinforced concrete; carbonation, corrosion; cracking; phase field.

1. Introduction

One of the most frequent and serious degradation process in reinforced concrete (RC) elements is the corrosion of the reinforcement bars (rebars) (Ahmad, 2003; Rodrigues et al., 2021). The continuous deterioration of material

* Corresponding author.
E-mail address: francesco.freddi@unipr.it

characteristics caused by corrosion has a significant impact on the serviceability and durability of structures, raising serious safety concerns (Bertolini et al., 2013; Bossio et al., 2019; Fernandez et al., 2016; Sun et al., 2020). In fact, corrosion of the rebar produces waste materials which generate overpressures on the surrounding concrete, potentially leading to cover cracking and spalling phenomena which expose the steel reinforcements to the outer environment. Moreover, the cross-sectional area of the rebar is progressively reduced, compromising the structure's bearing capacity and ductility.

Due to its importance, corrosion impacts on reinforced concrete structures have been the subject of numerous studies (Andrade, 2007; Rodrigues et al., 2021; Tuutti, 1982). To replicate and investigate the rusting process, extensive experimental tests were conducted (Andrade et al., 1993; Choe et al., 2020; Nguyen et al., 2011; Ouglova et al., 2008; Verma et al., 2014) to cite a few. Several analytical models have been proposed starting from experimental data to describe various aspects of the deterioration process. Models for cracking caused by the volume expansion of corroded rebars are illustrated in (Andrade et al., 1993; Bhargava et al., 2006; Imperatore & Rinaldi, 2019; X. Lin et al., 2017), whereas in (Imperatore et al., 2017; Ou et al., 2016) a correlation between the corrosion evolution and the degradation of mechanical properties of the steel are determined. Predictive numerical models have also been used to evaluate the impacts of corrosion on RC elements. In (Ansari et al., 2018; Clarelli et al., 2014; Mai et al., 2016; Sheng & Xia, 2017) different approaches for steel corrosion have been provided, as well as predictions of cracking mechanisms in the concrete cover are illustrated in (G. Lin et al., 2010; Molina et al., 1993; Richard et al., 2010, 2016; Zhang & Su, 2020).

In this work, a phase-field model describing the rupture in RC elements subjected to carbonation process and corrosion of rebar is proposed. The main focus is to develop a predictive model which, based on the numerical implementation of the physical equations which govern the different phenomena of the degradation process, can describe accurately the concrete cover cracking and spalling starting from the external environmental conditions affecting the structure.

The penetration of air pollutants into the concrete cover and the associated carbonation process are described via a reaction-diffusion system of equations (Bonetti et al., 2019, 2021; Giavarini et al., 2008; Isgor & Razaqpur, 2004; Papadakis et al., 1991a). Eventually, as the carbonation front approaches the rebars the protective passive layer around the steel dissolves, leading to the initiation of the corrosion process (Isgor & Razaqpur, 2006; Popov, 2015). Via the usage of electrochemistry equations (Bažant, 1979b; Hunkeler, 1997; Petre-Lazar, 2000), the amount of oxidation products formed due to corrosion are determined, and the corresponding volumetric expansion tied to the formation of rust deposits around the rebar is considered as loading parameter in the mechanical problem. Lastly, the fracture problem is investigated via the phase field approach for brittle fracture (Bourdin et al., 2000; Bui & Hu, 2021; J.-Y. Wu et al., 2019; Zhuang et al., 2022) which describes the nucleation and propagation of cracks via the minimization of a two-field functional, namely the displacement field and the damage state of the solid. The phase-field method permits to replicate a wide range of failure patterns, such as traction/compression asymmetric damaging behavior (Amor et al., 2009; Freddi & Royer-Carfagni, 2010, 2011), shear fracture (Alessi et al., 2020; Lancioni & Royer-Carfagni, 2009), cohesive (Freddi & Iurlano, 2017), porous material (Chukwudozie et al., 2019) and ductile materials (Alessi et al., 2014, 2015; Freddi & Royer-Carfagni, 2014, 2016). In recent years, due its versatility and its capability to accurately represent fractures within a body without any a-priori knowledge on the crack location, the phase-field model has also been used to investigate damaging of concrete elements under different deterioration processes. In (J. Y. Wu & Chen, 2022) the concrete deterioration induced by the coupling of calcium leaching and fracture has been analyzed. Cracking of the concrete due to chloride diffusion has been studied in (T. Wu & de Lorenzis, 2016; Yu & Jin, 2020) while a meso-scale model which describes the concrete cover cracking using the phase-field approach has been presented in (Fang et al., 2022; Hu et al., 2022).

By coupling the different physical processes that characterize the carbonation induced corrosion cracking, the deterioration process of the reinforced concrete is analyzed. A numerical model which considers the interactions between each phenomenon has been developed in order to investigate the cover cracking and spalling process. After validation against experimental data, some numerical simulations illustrate the capabilities of the predictive model to replicate fracture processes in RC elements due to rebars corrosion.

Nomenclature

[i]	concentration of the i-th species [mol/mm^3]
φ	carbonation state of the concrete
$\xi(\varphi)$	concrete porosity as a function of the carbonation state
f	volume fraction of pores corresponding to the liquid phase
f_w	volume fraction of the pores occupied by the film of water
D_{CO2}	diffusion coefficient of the carbon dioxide [mm^2/day]
r_n	neutralization reaction rate
RH	relative humidity
H	Henry constant for the dissolution of CO_2(g) in water ($34.2\cdot10^{-9}$ [mol/mm^3] at 25°C)
R	universal gas constant ($8.2057\cdot10^4$ [mm^3·atm / K·mol])
T	absolute temperature [K]
k_2	rate constant of reaction of CO2 and OH- (8.3·109 [mm3 / mol·s])
$[OH^-]_{eq}$	molar concentration of OH^- at equilibrium ($43.2\cdot10^{-9}$ [mol/mm^3] at 25°C)
$P(\varphi)$	material modulation functions
E_0	standard electric potential of the semi-reaction [V / SHE]
n	number of electrons involved in the cell reactions
F	Faraday constant (96485.33 [s·A / mol])
$b_{a/c}$	Tafel slope coefficient for the anode/cathode reaction
$i^0_{Ox/R}$	current density of the oxidation / reduction semi-reaction [A/mm^2]
$E_{Ox/R}$	electric potential of the oxidation / reduction semi-reaction [V]
i_{Corr}	corrosion current density [A / mm^2]
r	rebar radius [mm]
PA_{Fe}	iron atomic weight
ρ_{Fe}	iron density [g/mm^3]
γ	iron to rust density ratio
β	iron to rust molar mass ratio
$\mathbf{u}$	displacement field
α	damage field
$\boldsymbol{\varepsilon}$	strain tensor
G_c	fracture toughness [N/mm]
ℓ	internal length parameter [mm]
λ	first Lamè parameter
μ	second Lamè parameter
k_c	coercivity constant
$\mathbb{C}$	fourth order elasticity tensor

2. Carbonation induced corrosion cover cracking

Carbonation-induced corrosion cover cracking is a complex deterioration phenomenon that involves three key mechanisms: concrete carbonation, steel rebar corrosion and expansion, and concrete cover cracking. In this section the main aspects of these processes are illustrated.

A RC element $\Omega \in \mathbb{R}^d$ $(d = 1,2,3)$ with imposed displacements $\overline{\mathbf{u}}$ on the boundary portion $\partial\Omega^u$ is considered. The mechanical state of the materials of Ω, concrete OR steel, is fully determined by the displacement field **u** and a material scalar damage variable α: Ω→[0, 1] which can be seen as a phase field: α equal to 0 represents the sound material whereas value equal to 1 is assumed in the areas where cohesion is fully lost. Cracks within the materials are smeared; a transition zone from the sound to completely broken solid is determined by an internal length scale parameter ℓ. Cracks in this case are caused by the expansion of rebar due to the corrosion process induced by the carbonation process of concrete. These phenomena must be calculated and coupled with the mechanical problem.

The section is organized as follows. Firstly, the carbonation process is introduced. After, the expansion of the rebar due to rust formation is determined and finally the phase field approach for brittle fracture is presented.

2.1. Carbonation

Considering a standard fully hydrated ordinary Portland cement (OPC) concrete (Bullard et al., 2011), the main responsible of the carbonation process is carbon dioxide (CO_2). After entering the concrete in a gaseous state through the surface pores, it dissolves in the pore water and reacts with the calcium hydroxide ($Ca(OH)_2$) of the cement paste producing calcium carbonate ($CaCO_3$). In the following, the state of a component can be gaseous (g), liquid (aq) or solid (s). The reactions occur after both the carbon dioxide and the calcium hydroxide change to liquid state by dissolving within the concrete pore water as stated by the following reactions for the carbon dioxide

$$H_2O + CO_2(g) \rightarrow HCO_3^-(aq) + H^+(aq) \quad (1)$$
$$HCO_3^-(aq) \rightarrow CO_3^{2-}(aq) + H^+(aq)$$

and for the calcium hydroxide

$$Ca(OH)_2(s) \rightarrow Ca^{2+}(aq) + 2OH^-(aq) \quad (2)$$

Eventually, the neutralisation process takes place, resulting in the production of $CaCO_3$.

$$Ca^{2+}(aq) + 2OH^-(aq) + CO_3^{2-}(aq) + 2H^+(aq) \rightarrow CaCO_3(s) + 2H_2O \quad (3)$$

The carbonation process described by equations (1)-(3) takes place if the relative humidity in concrete is between 50% and 70%. Lower values prevent CO_2 from completely dissolving in water, whereas larger values significantly restrict CO_2 diffusion via concrete pores. After the neutralization reaction, calcium carbonate accumulates in the concrete pores due to its lower solubility compared to calcium hydroxide, clogging them and reducing the porosity of the material. A different behavior is observed if a blended cement, such as BFS or fly ash concrete, is considered. Here, due to the low content of the calcium hydroxide, the main contribution to the carbonation process is given by the C-S-H phase. As a results, the neutralization reaction occurs at a slower rate and different changes to the material properties such as an increase in porosity and a higher gas and fluid permeability can be observed (Johannesson, 1997; Isgor & Razaqpur, 2004).

To characterize the evolution of the carbonation process within the specimen, the carbonation front φ is described as the percentage of initial calcium hydroxide consumed (Isgor & Razaqpur, 2004), and it is expresses as follows

$$\varphi = 1 - \frac{[Ca(OH)_2]}{[Ca(OH)_2]^0} \quad (4)$$

Moreover, due to the formation of $CaCO_3$, the concrete's mechanical properties are modified. To account for the changes of a generic material property P, which changes from P_c to P_{CaCO3} after the carbonation process, a linear relationship between the carbonation profile and the change in the parameters value is considered as reported in the following equation

$$P(\varphi) = P_c + \varphi(P_{CaCO_3} - P_c) \quad (5)$$

From the mathematical point of the view, the carbonation process is reproduced via a diffusion-reaction equation system (Papadakis et al., 1991a). The evolution of the concentration of the carbon dioxide $[CO_2]$ within the concrete is obtained by solving the following equation which derives from the Fick's second diffusion law

$$\frac{\partial}{\partial t}[\xi(\varphi)(1-f)[CO_2]] = \nabla \cdot (D(\varphi,\alpha)\,\nabla[CO_2]) - \xi(\varphi) f_w r_n \quad (6)$$

The term $\xi(\varphi)(1-f)$ multiplying the gaseous concentration of $[CO_2]$, refers to the unit volume of the gas-phase within the pores, being $\xi(\varphi)$ the porosity depending on the carbonation front location φ and f the volume fraction of the pores corresponding to the liquid phase. The reaction term is obtained as the product of the neutralization rate r_n and $\xi(\varphi)f_w$ which represents the unit volume of pores partially filled with water and partially with air, being f_w the corresponding volume fraction of the pores. The values of f and f_w can be obtained using the analytical equations as well as the experimental results reported in (Papadakis et al., 1991b) starting from the pore size distribution of the hardened cement paste, the ambient relative humidity and temperature.

The diffusion coefficient $D_{CO_2}(\varphi,\alpha)$ depends on the carbonation state due to the changes of the porosity and on the damage state of the material. The value for the undamaged diffusion coefficient for carbon dioxide within concrete has been studied in (Papadakis et al., 1991a), while the diffusion coefficient of the fully damaged material is assumed very high (~10^5) to account for an almost instantaneous diffusion of CO_2 within the fractures. The choice of this value is based on the fact that once a crack is fully developed, an opening is created with the outer environment. Depending on the type of external environmental condition (such as temperature, relative humidity, weather, ecc…) the behavior of the water, which greatly reduces the diffusion of the carbon dioxide within the cracks, differs. However, accounting for a variety of external environmental conditions is not a parameter we accounted on the current stage of the study. Therefore, an average condition of 25 °C and 65% of RH has been considered in the numerical simulations. With these settings, the film of water within cracks quickly evaporates leading to a free diffusive behavior of the carbon dioxide. A smooth variation in the value of the diffusion coefficient between concrete and cracks is ensured by the following expression

$$D(\varphi,\alpha) = \xi(\varphi)^{1.8}(1-RH)^{2.2}[1.42\cdot 10^{-6}(1-\alpha)^m + 10^5\alpha^m] \tag{7}$$

with $m = 10$ a coefficient controlling the nonlinear trend of variation of the diffusivity (T. Wu & de Lorenzis, 2016).

The neutralization reaction rate term r_n is given as a function of the molar concentration of the various reactants multiplied by the product between H, R, T and k_2 which are respectively the Henry constant for the dissolution of CO_2(g) in water, the universal gas constant, the absolute temperature and the rate constant of reaction of $[CO_2]$ and $[OH^-]$.

$$r_n = HRTk_2[OH^-]_{eq}[CO_2(g)][Ca(OH)_2(aq)] \tag{8}$$

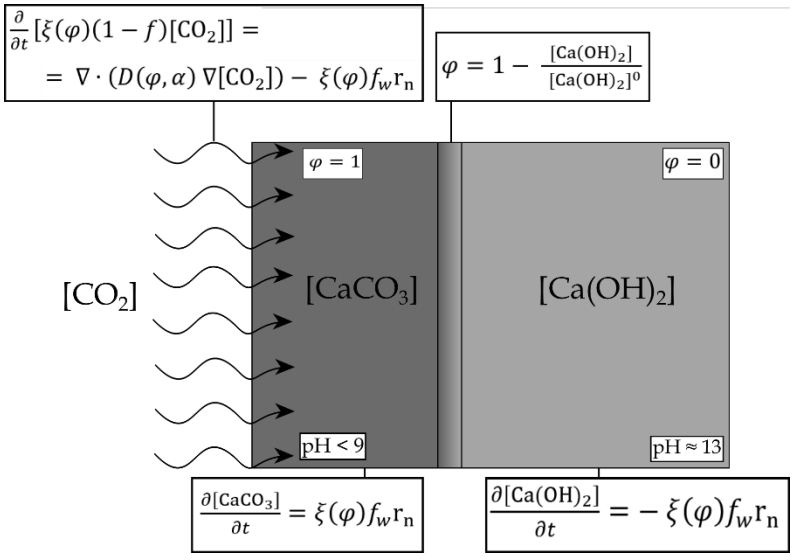

Fig. 1 Schematization of the carbonation model

For calcium hydroxide and calcium carbonate, only the reaction term is addressed and the resulting equations are respectively

$$\frac{\partial[\mathrm{Ca(OH)_2}]}{\partial t} = -\xi(\varphi) f_w \mathrm{r_n} \tag{9}$$

$$\frac{\partial[\mathrm{CaCO_3}]}{\partial t} = \xi(\varphi) f_w \mathrm{r_n} \tag{10}$$

The decrease of the pH value within the concrete is the key point of the carbonation process. While the hydration process of the cement paste creates an alkaline environment with a high pH (≈13), in which bars have a passive layer that protects them from corrosion, during the carbonation process the pH lowers to more neutral levels (<9) and causes de-passivation of the steel rebars, triggering the corrosion process.

The following equation is used to determine the pH of concrete (Papadakis et al., 1991a) starting from the concentration of $\mathrm{Ca(OH)_2}$

$$\mathrm{pH} = 14 + \log\left(2 \cdot 10^3 [\mathrm{Ca(OH)_2}]\right) \tag{11}$$

2.2. Corrosion

Whenever the carbonation front approaches the bar surface, the pH of concrete drops to neutral level, causing the protective passive layer to dissolve. The de-passivation of the steel bars along its length is uniform due to the homogenous progression of the carbonation front. As a result, a microcell corrosion system develops in which multiple anodic and cathodic zones are formed in close proximity (Hansson et al., 2006) covering the whole length of the depassivated portion of the rebar (Fig. 2). Corrosion is an electrochemical process in which rebars are degraded by anodic dissolution of steel into pore water in response to the semi-reaction

$$\mathrm{Fe} \rightarrow \mathrm{Fe^{2+}} + 2\mathrm{e^-} \tag{12}$$

The two free electrons of reaction (13) are used in the cathodic oxygen reduction nearby the steel rebar

$$\frac{1}{2}\mathrm{O_2} + \mathrm{H_2O} + 2\mathrm{e^-} \rightarrow 2\mathrm{OH^-} \tag{13}$$

Since the corrosion process is developed over a microcell corrosion system in which the anodic and cathodic sites are in close proximity, the dissolved iron ions of eq. (12) and the hydroxides of eq. (13) are consumed locally, leading to the complete reaction which defines the corrosion mechanism of steel (Broomfield, 2003)

$$\begin{aligned} &\mathrm{Fe^{2+}} + 2\mathrm{OH^-} \rightarrow \mathrm{Fe(OH)_2} \\ &4\mathrm{Fe(OH)_2} + \mathrm{O_2} + 2\mathrm{H_2O} \rightarrow 4\mathrm{Fe(OH)_3} \\ &4\mathrm{Fe(OH)_3} \rightarrow 2\mathrm{Fe_2O_3 \cdot H_2O} + 4\mathrm{H_2O} \end{aligned} \tag{14}$$

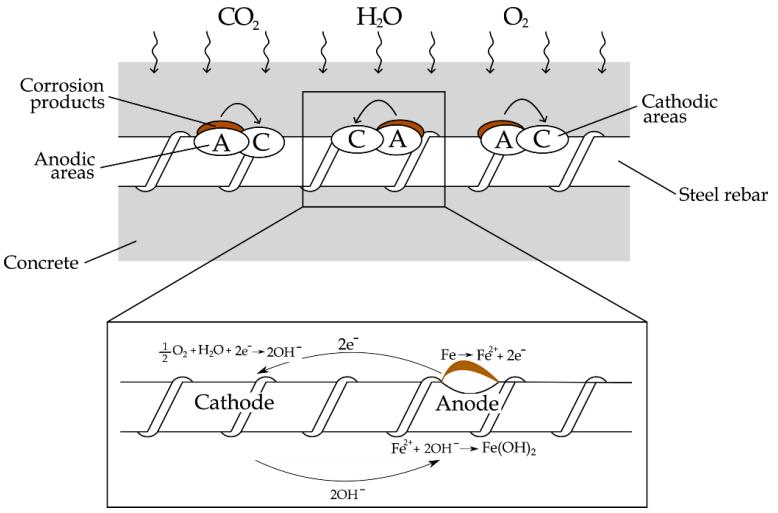

Fig. 2 Microcell corrosion system

Electrochemical kinetics equations are adopted to model the corrosion process (Popov, 2015). The first step is to use the Nernst equation to calculate the electric potential for each of the semi-reactions (13)-(14)

$$\mathrm{E}_{Fe|Fe^{2+}} = \mathrm{E}_{0,Fe|Fe^{2+}} + 2.303\frac{RT}{nF}\log\left[Fe^{2+}\right] \qquad (15)$$

$$\mathrm{E}_{O_2|OH^-} = \mathrm{E}_{0,O_2|OH^-} - 2.303\frac{RT}{nF}\log\left[OH^-\right]$$

where $\mathrm{E}_{0,Fe|Fe^{2+}}$ and $\mathrm{E}_{0,O_2|OH^-}$ are the standard electric potentials of the anodic and cathodic semi-reaction [V/SHE] respectively, R is the universal gas constant ($8.2057\cdot10^4$ [mm^3·atm / K·mol]), T is the temperature [K], n is the number of electrons involved in the cell reactions, F is the Faraday constant (96485.33 [s·A / mol]) and $[Fe^{2+}]$ and $[OH^-]$ are the concentrations of the oxidized and reduced species [mol / mm^3]. While the hydroxide concentration is known from the pH evaluated with eq. (11), since the electric charge in the pore solution has to be in balance (Bažant, 1979a), the molar concentration of the iron which dissolves during the anodic process can be obtained via the stoichiometry coefficients of eq. (12)-(13)-(14).

Since a microcell corrosion system is considered, the distance between the anodic and cathodic region is assumed to be sufficiently small such that the ohmic drop associated with the ions transfer between the anode and cathode can be neglected. Moreover, a common outdoor not-submerged structure has been considered and therefore no reduction of the corrosion rate induced by limited oxygen diffusion is expected (Huet et al., 2007; Raupach, 1996a, 1996b). Therefore, using the values of the half-cell potentials (E_R, E_{Ox}), the anode and cathode Tafel slope coefficients (b_a, b_c) and the current density of the semi-reactions (i_R^0, i_{Ox}^0), the corrosion current density can be evaluated by rearranging the Butler-Volmer equation at the equilibrium state from the electric potential distribution on the surface of the rebar (Popov, 2015).

$$i_{Corr} = \exp\left\{\frac{(\mathrm{E}_R - \mathrm{E}_{Ox}) - \mathrm{b}_c\log(i_R^0) + \mathrm{b}_a\log(i_{Ox}^0)}{\mathrm{b}_a - \mathrm{b}_c}\right\} \qquad (16)$$

Starting from the corrosion current density distribution around the rebar, the associated mass loss can be obtained via the Faraday's law of electrolysis. Using the iron density ρ_{Fe}, the iron to rust density ratio γ ($\rho_{\mathrm{Fe}}/\rho_{\mathrm{Fe_2O_3}}$) and the iron to rust molar mass ratio β ($\mathrm{PA_{Fe}}/\mathrm{PA_{Fe_2O_3}}$) it is possible to convert the mass loss into the equivalent change in radius due to the formation of rust as reported in the equation below

$$\mathrm{dr} = \left\{\frac{i_{Corr}(2\pi r\ L)\ \mathrm{PA_{Fe}}}{nF\rho_{\mathrm{Fe}}}\right\}\left(\frac{\gamma}{\beta}-1\right)\ \mathrm{dt} \tag{17}$$

where i_{Corr} is the corrosion current density, L is the unit length of the rebar and $\mathrm{PA_{Fe}}$ is the molar mass of iron.

Lastly, being $\mathbb{I} \in \mathbb{R}^d$ $(d = 1,2,3)$ the identity tensor of rank d, the deformation tensor associated with the rebar expansion is evaluated at each point of the depassivated portion of the rebar from the ratio between the change in radius and the initial radius as given by the following equation

$$\boldsymbol{\varepsilon_0} = \frac{\mathrm{dr}}{\mathrm{r}}\mathbb{I} \tag{18}$$

2.3. Cracking

As the steel rebar corrodes, rust deposits create overpressures on the surrounding concrete. Cracks nucleate and propagate once the concrete traction resistance is exceeded. Complex fracture pattern may emerge, resulting in spalling, which occurs when the concrete cover is expelled from the element.

The crack nucleation and propagation in the concrete are determined via the minimization of an energy functional that depends on the displacement field **u** and the damage field α. Only a brief discussion is presented here to facilitate comprehension of the work. The method's detailed overview may be found in (Bourdin et al., 2000; Bui & Hu, 2021; J.-Y. Wu et al., 2019; Zhuang et al., 2022).

The total potential energy functional is computed as the sum of two contributions based on the strain and fracture energy densities. The strain energy density has been separated into three parts to account for the different materials: one associated to concrete, one to steel and other to rust. The traction/compression asymmetric damaging behaviour of concrete is embedded by splitting the strain energy density into a positive and negative parts according to the approach proposed in (Freddi & Royer-Carfagni, 2011)

$$\begin{aligned}\psi_c^+(\boldsymbol{\varepsilon},\alpha,\varphi) &= ((1-\alpha)^2 + k_c)\,\tfrac{1}{2}\,\boldsymbol{\varepsilon}_+ : \mathbb{C}_c(\varphi) : \boldsymbol{\varepsilon}_+ \\ \psi_c^-(\boldsymbol{\varepsilon},\varphi) &= \tfrac{1}{2}\,\boldsymbol{\varepsilon}_- : \mathbb{C}_c(\varphi) : \boldsymbol{\varepsilon}_-\end{aligned} \tag{19}$$

To facilitate rupture in the material to occur under tensile stresses, the degradation function $(1-\alpha)^2 + k_c$, with k_c (~10^{-6}) a coefficient introduced to render coercive the strain energy functional, is applied only to the positive part of the strain energy. Since the negative part of the strain energy is not affected from the phase-field, compression stresses are still present and transmitted through cracks, implicitly introducing a unilateral contact effect between the two portions of the material divided by a crack under closure. $\boldsymbol{\varepsilon}_+$ and $\boldsymbol{\varepsilon}_-$ are the positive and negative part of the deformation tensor, appositely determined starting from the following decomposition of the deformation tensor

$$\boldsymbol{\varepsilon} = \sum_{i=1}^{d} \varepsilon_i\, \boldsymbol{n_i} \otimes \boldsymbol{n_i} \tag{20}$$

where ε_i are the ordered eigenvalues ($\varepsilon_i \geq \varepsilon_{i+1}$) and $\boldsymbol{n_i}$ the corresponding eigenvectors. Considering the case for a plain strain condition with d = 2, the positive and negative deformation tensors are defined as follows

$$\begin{aligned}&if\ \varepsilon_2 \geq 0 \\ &\qquad \boldsymbol{\varepsilon}^+ \leftarrow \boldsymbol{\varepsilon} \\ &\qquad \boldsymbol{\varepsilon}^- \leftarrow \mathbf{0} \\ &if\ (1-\upsilon)\varepsilon_1 + \upsilon\varepsilon_2 > 0\ and\ \varepsilon_2 < 0 \\ &\qquad \boldsymbol{\varepsilon}^+ = \begin{bmatrix} \varepsilon_1 + \dfrac{\upsilon}{1-2\upsilon}\varepsilon_2 & 0 \\ 0 & 0 \end{bmatrix}\end{aligned} \tag{21}$$

$$\boldsymbol{\varepsilon}^{-} = \begin{bmatrix} -\frac{\upsilon}{1-2\upsilon}\varepsilon_2 & 0 \\ 0 & \varepsilon_2 \end{bmatrix}$$

$if\ (1-\upsilon)\varepsilon_1 + \upsilon\varepsilon_2 \leq 0$

$$\boldsymbol{\varepsilon}^{+} \leftarrow \mathbf{0}$$
$$\boldsymbol{\varepsilon}^{-} \leftarrow \boldsymbol{\varepsilon}$$

Detailed description of this formulation is given in (Freddi & Royer-Carfagni, 2010, 2011). $\mathbb{C}_c(\varphi)$ is the classical fourth order elasticity tensor for concrete depending on the Lame's parameters. In addition, to account for the change of the concrete mechanical properties due to the carbonation process, the Lame's parameters used to evaluate the elasticity tensor change according to the linear variation given by eq. (5).

The strain energy expression of steel ψ_s is classical whereas the strain energy of the rusted portion of steel ψ_r includes the inelastic deformation tensor $\boldsymbol{\varepsilon_0}$ due to the rust deposit over the rebar and calculated via eq. (18)

$$\psi_s(\varepsilon) = \frac{1}{2}\,\boldsymbol{\varepsilon}\colon\mathbb{C}_s\colon\boldsymbol{\varepsilon} \tag{22}$$

$$\psi_r(\varepsilon,\varepsilon_0) = \frac{1}{2}\,(\boldsymbol{\varepsilon} - \boldsymbol{\varepsilon}_0)\colon\mathbb{C}_r\colon(\boldsymbol{\varepsilon} - \boldsymbol{\varepsilon}_0) \tag{23}$$

being $\mathbb{C}_s$ and $\mathbb{C}_r$ the classical fourth order elasticity tensor for steel and rust respectively. The value of ψ_r is evaluated only over the rust layer elements which are determined by checking the value of the pH over the steel rebar surface.

Lastly, the fracture energy density $\Psi(\alpha,\varphi)$, is introduced to complete the phase-field formulation.

$$\Psi(\alpha,\varphi) = \frac{3}{8}\,\mathrm{G}_c\,\left(\frac{\alpha^2}{\mathrm{d}_\ell(\varphi)\,\ell} + \mathrm{d}_\ell(\varphi)\,\ell\,\|\nabla\alpha\|^2\right) \tag{24}$$

This term accounts for the energy dissipated by the formation of damage and is proportional to the crack length via the fracture toughness $\mathrm{G_c}$. Here, the parameter ℓ is a length scale which governs the width of the smeared cracks representation and can be treated as a material parameter (Tanné et al., 2018). Therefore, following eq. (5) which provides the linear variation for the material properties change due to the carbonation process, the term $\mathrm{d}_\ell(\varphi)$ is introduced. In eq. (24) the first term $\alpha^2/\mathrm{d}_\ell(\varphi)\,\ell$ represents the local part and determines the distribution of the phase-field while the second term $\mathrm{d}_\ell(\varphi)\,\ell\,\|\nabla\alpha\|^2$ denotes the nonlocal part that incorporates the length scale ℓ. Other possible choices for the first term could be also employed (Borden et al., 2014; Pham et al., 2011).

Eventually, by adding together the energetic contribution of each domain given by eq. (19)-(22)-(23)-(24), the following total energy functional is obtained

$$\Pi_\ell(\varepsilon,\varepsilon_0,\alpha,\varphi) = \int_{\Omega_c}[\psi_c^{+}(\boldsymbol{\varepsilon},\alpha,\varphi) + \psi_c^{-}(\boldsymbol{\varepsilon},\varphi)]\,\mathrm{d}\mathbf{x}_c + \int_{\Omega_s}\psi_s(\boldsymbol{\varepsilon})\,\mathrm{d}\mathbf{x}_s + \int_{\Omega_r}\psi_r(\boldsymbol{\varepsilon},\boldsymbol{\varepsilon}_0)\,\mathrm{d}\mathbf{x}_r + \int_{\Omega_c}\Psi(\alpha,\varphi)\;\mathrm{d}\mathbf{x}_c \tag{25}$$

The evolution of the fracture within the solid is obtained by solving the minimization problem of the total energy functional, given by

$$\min_{(\mathbf{u},\alpha)\in D}\Pi_\ell(\boldsymbol{\varepsilon},\alpha)\,;\quad D = \{(\mathbf{u},\alpha)\in W^{1,2}(\Omega,\mathbb{R}^d)\;\times\;W^{1,2}(\Omega,[0,1]) : \mathbf{u} = \overline{\mathbf{u}}\ \text{on}\ \partial\Omega^u\} \tag{26}$$

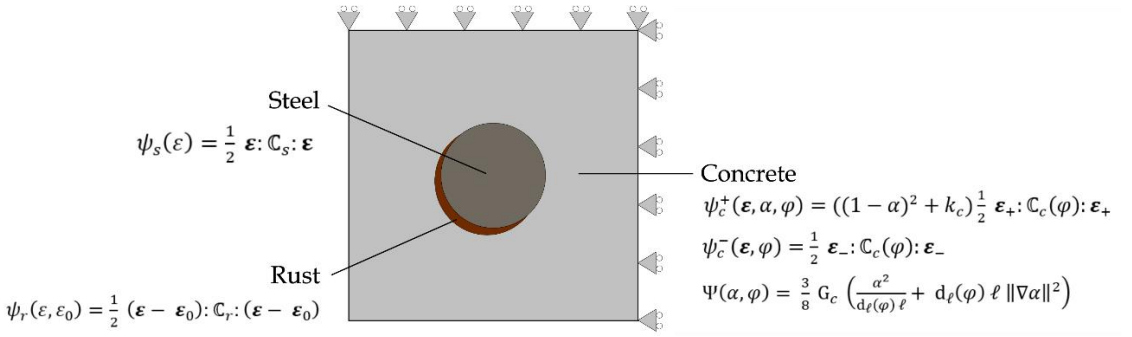

Fig. 3 Mechanical problem domains and their corresponding energy functionals

The Euler-Lagrange equations are derived by differentiating the energy functional with respect to the strain tensor and phase-field.

$$\begin{cases} \operatorname{div}\mathbf{T} = 0 \\ \frac{3}{4}\frac{G_c\,\alpha}{d_\ell(\varphi)\,\ell} + \frac{3}{4}G_c\,d_\ell(\varphi)\,\ell\,\Delta\alpha - (1-\alpha)\,\boldsymbol{\varepsilon}_+:\mathbb{C}_c(\varphi):\boldsymbol{\varepsilon}_+ = 0 \end{cases} \tag{27}$$

being **T** the Cauchy stress tensor equal to

$$\mathbf{T} = \frac{\partial\psi_c^+(\boldsymbol{\varepsilon},\alpha,\varphi)}{\partial\boldsymbol{\varepsilon}} + \frac{\psi_c^-(\boldsymbol{\varepsilon},\varphi)}{\partial\boldsymbol{\varepsilon}} + \frac{\psi_s(\boldsymbol{\varepsilon})}{\partial\boldsymbol{\varepsilon}} + \frac{\psi_r(\boldsymbol{\varepsilon},\boldsymbol{\varepsilon}_0)}{\partial\boldsymbol{\varepsilon}} \tag{28}$$

To prevent the material healing, an irreversibility condition is applied to the damage field. The Euler-Lagrange equations are replaced by the following Karush-Kuhn-Tucker conditions.

$$\begin{cases} \frac{3}{4}\frac{G_c\,\alpha}{d_\ell(\varphi)\,\ell} + \frac{3}{4}G_c\,d_\ell(\varphi)\,\ell\,\Delta\alpha - (1-\alpha)\,\boldsymbol{\varepsilon}_+:\mathbb{C}_c(\varphi):\boldsymbol{\varepsilon}_+ \le 0 \\ \dot{\alpha} \ge 0 \\ \left(\frac{3}{4}\frac{G_c\,\alpha}{d_\ell(\varphi)\,\ell} + \frac{3}{4}G_c\,d_\ell(\varphi)\,\ell\,\Delta\alpha - (1-\alpha)\,\boldsymbol{\varepsilon}_+:\mathbb{C}_c(\varphi):\boldsymbol{\varepsilon}_+\right)\dot{\alpha} = 0 \end{cases} \tag{29}$$

3. Numerical solution

The proposed model involves the solution of time dependent partial differential equations. A fully implicit finite element scheme has been adopted in which the simulated time interval [0, T] has been subdivided into equal-sized small time increment Δt.

At a given time increment, the first step of the model consists in the evaluation of the carbonation process by calculating the updated concentration of [CO2], [Ca(OH)2] and [CaCO3] via the numerical solution of equations (6)-(9)-(10). The damage field obtained from the solution of the mechanical problem at the previous time step is considered in eq. (7) for the evaluation of the diffusion coefficient. From the updated concentration of the carbon dioxide, the change in the carbonation front is determined using eq. (4) and the material parameters of the concrete are modified accordingly to eq. (5). The variation of the pH within the cement paste is obtained from eq. (11).

Once the value of the pH at any gauss point of the outer elements of the rebar becomes lower than 9, the corrosion process starts. The interested elements are therefore converted into rust and their material properties change accordingly (De Jong et al., 2015). For the rust elements, the anodic and cathodic electric potentials are evaluated with eq. (15). Eventually, the corrosion current density is obtained using eq. (16), the radius expansion and the associated swelling with eq. (17)-(18) respectively. Being rust a porous material, water and oxygen present in the surrounding of

the steel rebar can penetrate into the rust layer and the corrosion front moves toward the inner portion of the steel rebar, reducing its cross section. Following (Huet et al., 2007), the diffusion properties of the oxide layer has been assumed to be equal to the one of the carbonated concrete.

Lastly, using the swelling of the rust elements as a loading parameter for the mechanical problem, the damage state in the carbonated concrete is obtained by solving the Euler-Lagrange equation (27)a coupled with the constrained evolution equations (29) using of a staggered multi-step algorithm (Mesgarnejad et al., 2015).

Fig. 4 reports the flowchart detailing the steps which are performed at each time increment. All the numerical simulations have been performed using the open-source finite element computing platform for solving partial differential equations DEAL.II (Arndt et al., 2021; Bangerth et al., 2007).

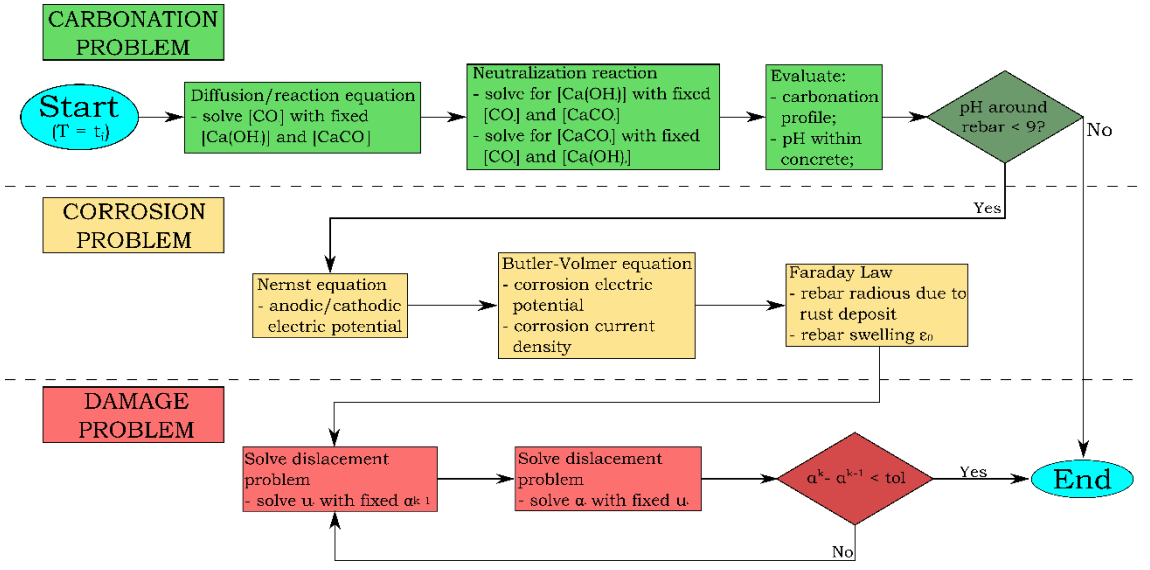

Fig. 4 Flowchart of the numerical method

4. Numerical tests

In the section the proposed model is validated against experimental results available in literature and subsequently two fracture tests have been proposed.

4.1. Model validation

In (Papadakis et al., 1991a), the carbonation process of a concrete specimen is experimentally investigated. A rectangular specimen with size L = 300 mm and H = 100 mm of ordinary Portland concrete with a w/c ratio equal to 50% at 65% RH is considered. CO_2 at 50% concentration and room temperature (30°C) penetrates into the specimen according to scheme of Fig 5 from the left vertical side. The carbonation front's location is obtained numerically with the solution of equations (6)-(9)-(10)-(4) and reported in Table 1 together with experimental and numerical results available in literature at different times. The results obtained using the proposed approach is in good agreement with the literature.

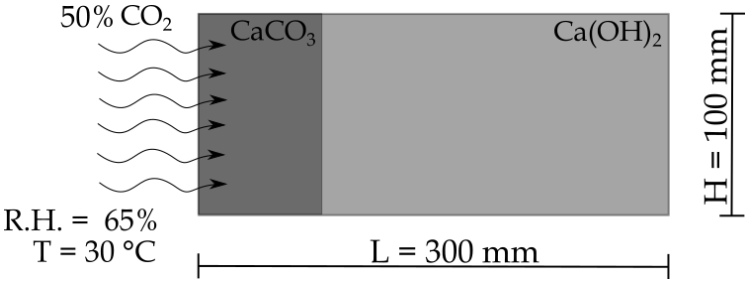

Fig. 5 Domain used for the validation of the carbonation model

Table 1. Carbonation depth results comparison

Days	Experimental results [mm] (Papadakis et al., 1991a)	Numerical results [mm] (Papadakis et al., 1991a)	Numerical results [mm]
1	3	3.5	3.3
3	5	5.5	4.5
5	8	7	6.6
10	10	8.9	9.3
15	12	11.5	11.4
20	15	14	14.4

Furthermore, the corrosion process outcomes are examined and compared to average corrosion current density data for reinforcement bars with a passive layer ($i_{corr} < 0.1$ μA/cm^2), and without passive layer ($i_{corr} \approx 1$ μA/cm^2) reported in (Medagoda Arachchige, 2008; Stefanoni et al., 2018). A square domain of conventional Portland concrete with a 16 mm diameter bar with a side L = 76 mm is studied. The w/c ratio has been considered equal to 50% at 65% RH. At a temperature of 25 °C, an external concentration of 0.036% carbon dioxide is applied to the specimen's left and bottom sides as illustrated in Fig 6. The electrochemical parameters are listed in Table 2.

Table 2. Electrochemical parameters.

Parameters	Values
Anodic Tafel slope (b_a)	0.090 V/dec
Cathodic Tafel slope (b_c)	-0.180 V/dec
Anodic potential ($E_{0,a}$)	-0.440 V
Cathodic potential (E0,$_c$)	0.401 V
Anodic exchange current density (i_{Fe})	$3 \cdot 10^{-6}$ A/cm^2
Cathodic exchange current density (i_{O2})	$1 \cdot 10^{-7}$ A/cm^2

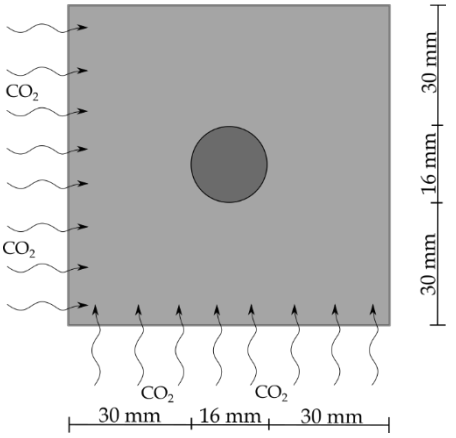

Fig. 6 Domain used for the validation of the corrosion model

The corrosion model gives results that are in good agreement with those presented in (Medagoda Arachchige, 2008): the corrosion current density for passivated steel rebar is equal to 0.097 $\mu A/cm^2$, rising to a constant value of 0.98 $\mu A/cm^2$ as the carbonation front reaches the rebar.

4.2. Double side diffusion test

A square specimen of ordinary Portland concrete, with w/c ratio of 50% and relative humidity of 60%, having dimension L = 76 mm and a 16 mm rebar in the center is now considered. CO_2 with concentration of 0.036% is set on the bottom and left side of the specimen boundary. Vertical and horizontal displacements are blocked on the top side and on the right side of the domain respectively (Fig. 7). Table 3 reports the concrete, steel and rust material parameters whereas the corrosion parameters are listed in Table 2. The simulated time is 20 years.

The results of the numerical simulation are reported in Figs. 8 and 9, showing the CO_2 concentration, the carbonation profile, the damage pattern, the rust deposits due to the rebar corrosion and the deformed configuration. The first row of Fig. 8 reports the results at the first crack nucleation (t = 2100 days) while the fourth row reports the results at the time of the concrete cover spalling (t = 2850 days). Two intermediate steps are reported in the two central lines of Fig. 8 (t = 2230, 2520 days).

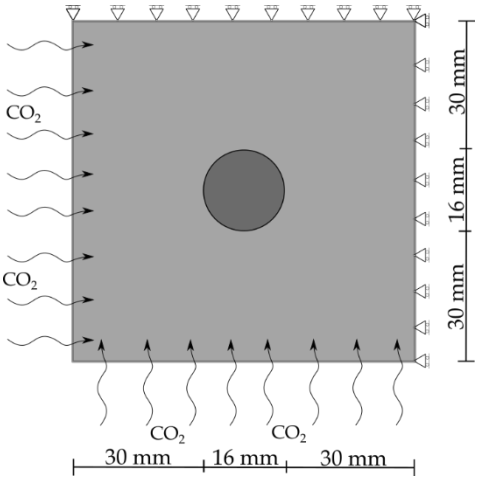

Fig. 7 Double side diffusion test setup

In particular, Fig. 7(b) shows the carbonation profile associated with the beginning of the cover cracking process, namely when the carbonation front reaches the steel rebar and the pH assumes values lower than 9. At this stage, corrosion begins over the depassivated portion of the steel rebar and the rust layer reported in Fig. 7(d) forms. Overpressures are generated in the surrounding concrete and once its traction resistance is reached cracks nucleate (Fig. 7(c)). As the process evolves, the corrosion moves toward the central portion of the steel section as visible in Fig. 7(h). The corresponding increase in corrosion products leads to increase of overpressures on concrete, causing the crack to propagate to the bottom edge of the specimen as reported in Fig. 7(g). Since the crack is directly connected with the external environment, carbon dioxide can easily enter the inner portion of the specimen (Fig. 7(e)), leading to the carbonation of the concrete surrounding the whole rebar. The passive layer around the rebar completely dissolves and the corrosion process affects its full perimeter as shown in Fig. 7(l). As a result, cracks propagate toward the upper edge of the domain (Fig. 7(k)) which results in the spalling of the left portion of the concrete cover as visible in the deformation plot of Fig. 8(b). Lastly, the complete spalling of the concrete cover is observed in Fig. 8(c) as cracks reach the right edge of the specimen (Fig. 7(o)).

Parameters	Values
Concrete elastic modulus (E_c)	31500 MPa
Concrete Poisson modulus (υ_c)	0.2
Concrete uniaxial traction strength (σ_{cT})	2.15 MPa
Concrete internal length parameter (ℓ_c)	5 mm
Steel elastic modulus (E_s)	210000 MPa
Steel Poisson modulus (υ_s)	0.3
Rust elatic modulus (E_r)	132000 MPa
Rust Poisson modulus (υ_r)	0.25
Carbonated concrete elastic modulus (E_{CaCO3})	35000 MPa
Carbonated concrete Poisson modulus (υ_{CaCO3})	0.2
Carbonated concrete uniaxial traction strength ($\sigma_{CaCO3,T}$)	4 MPa
Carbonated concrete internal length parameter (ℓ_{CaCO3})	4 mm

Table 3. Material parameters.

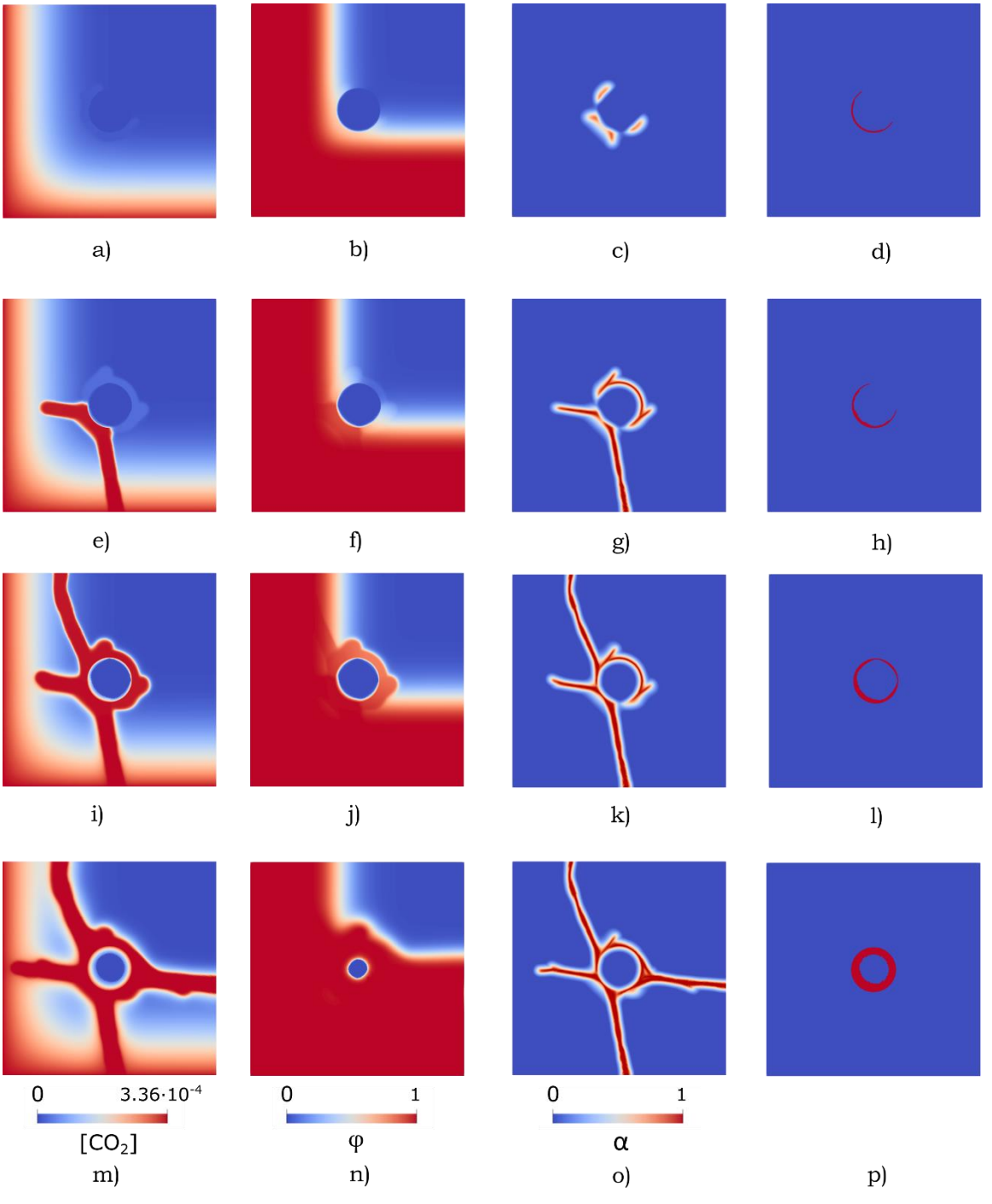

Fig. 8 Results for the double side diffusion test at different times: 1) crack nucleation; 2) cracking of the bottom edge; 3) spalling of the left portion of the concrete cover; 4) complete spalling of the concrete cover. The first column reports the carbon dioxide concentration, the second the carbonation profile, the third shows the crack pattern while the fourth column present the rust layer around rebar.

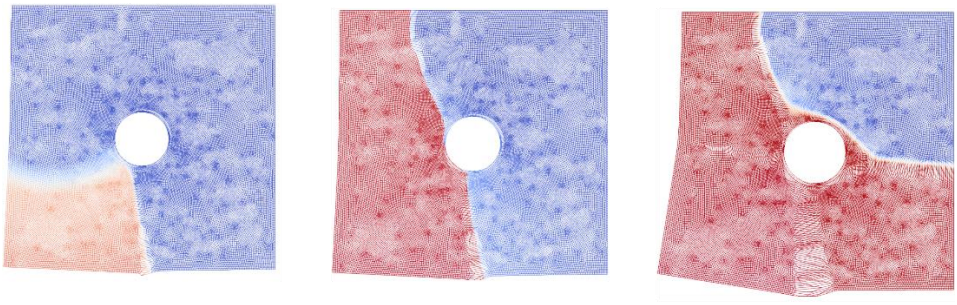

Fig. 9 Results for the double side diffusion test. Displacement field at different times: a) cracking of the bottom edge; b) spalling of the left portion of the domain; c) complete spalling of the concrete cover. The red portion of the mesh denotes the material expelled from the section.

4.3. Double side diffusion: three rebar specimen

The second test has been performed to evaluate the crack pattern in a three rebar specimen. The same parameters and boundary condition for the diffusion, corrosion and displacement problem adopted in the previous example have been assumed. The setup used for the test is reported in Fig. 10.

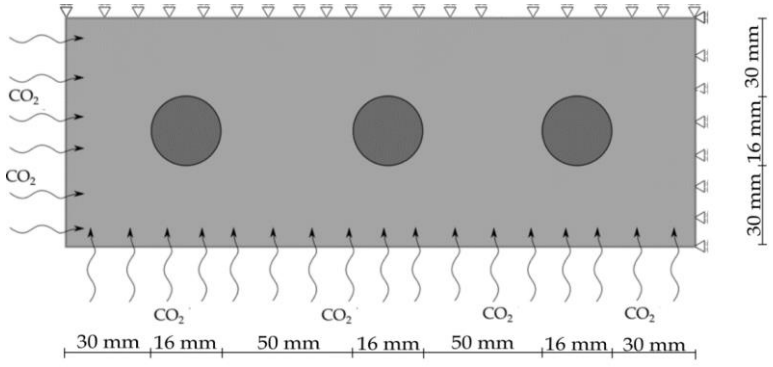

Fig. 10 Double side diffusion: three rebar specimen setup

Figs. 11, 12, 13, 14 and 15 show carbon dioxide diffusion, carbonation profile, crack pattern, rust deposits and displacement deformation respectively. Here, similarly to the previous example, the degradation process starts as the carbonation profile reaches the steel rebars (t = 2150 days). In fact, the corrosion process initiates over the depassivated steel leading to the nucleation and propagation of the first crack from the left rebar toward the bottom edge of the specimen (t = 2280 days). After this first cracking occurrence, with the advancement of the carbonation and corrosion processes, the presence of overpressure around the rebars due to the formation of rust deposits (Fig. 14(a)) leads to the debonding between the concrete and the left rebar while also propagating the fractures toward the central rebar as shown in Fig. 13(a) (t = 2600 days). Eventually, due to the capability of the CO_2 to freely diffuse through cracks (Fig. 11(a)), the carbonation process completely affects the concrete surrounding the central rebar, exacerbating its corrosion. Moreover, as the rust deposits increase in volume (Fig. 14(b)), cracks propagate toward the right rebar as reported in Fig. 13(b) leading to the spalling and expulsion of the concrete cover as shown in Fig. 15(b) (t = 2940 days).

Some numerical difficulties have been encountered in the resolution of this example. In fact, some excessive diffusion of the fully damaged portion of the material is evidenced in Fig 13(b). This phenomenon, that does not compromise the quality of the solution, occurs as the concrete surrounding a rebar is fully damaged thus leading to numerical singularities. A way to overcome this drawback is under investigation.

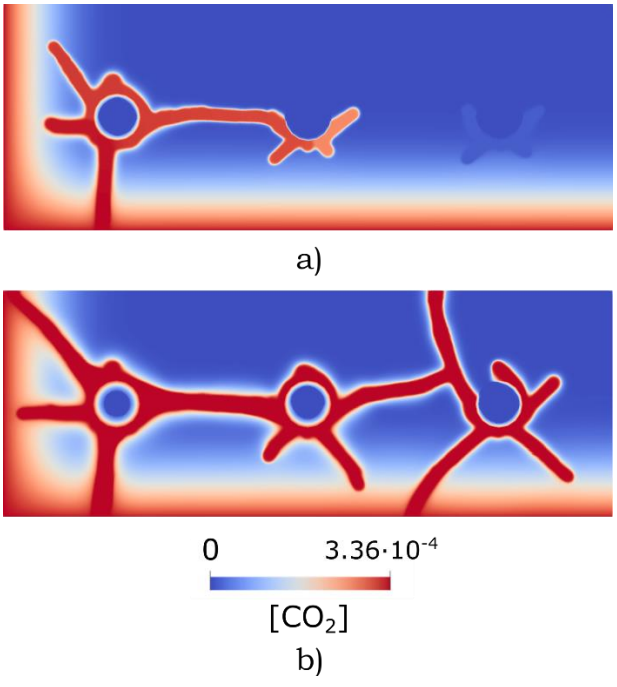

Fig. 11 Results for the double side diffusion test with three rebars. Carbon dioxide diffusion at different times: a) after the first internal crack propagation; b) before the expulsion of the concrete cover.

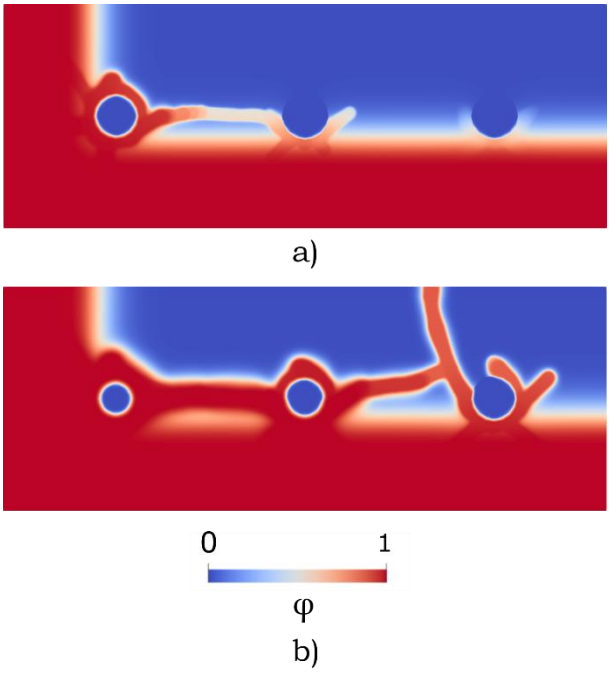

Figure 12 Results for the double side diffusion test with three rebars. Carbonation profile at different times: a) after the first internal crack propagation; b) before the expulsion of the concrete cover

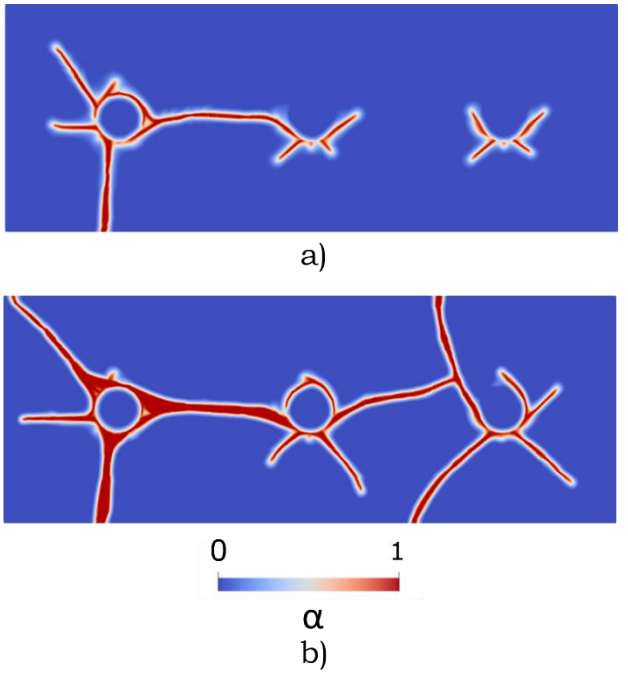

Figure 13 Results for the double side diffusion test with three rebars. Damage pattern at different times: a) first internal crack propagation; b) complete spalling of the concrete cover.

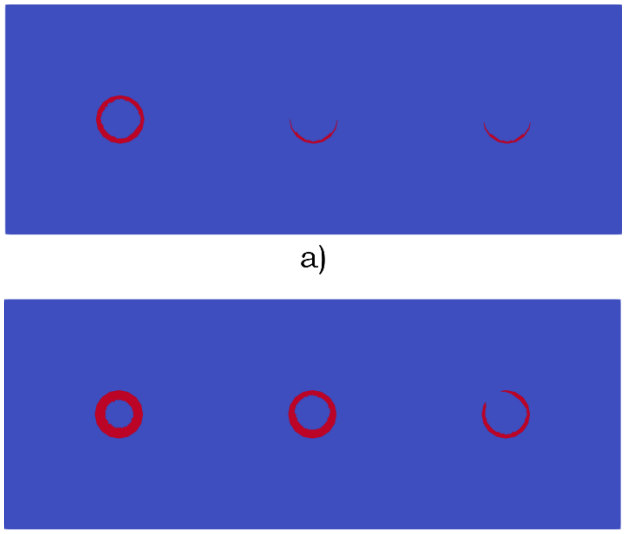

Figure 14 Results for the double side diffusion test with three rebars. Rust deposits at different times: a) first internal crack propagation; b) complete spalling of the concrete cover.

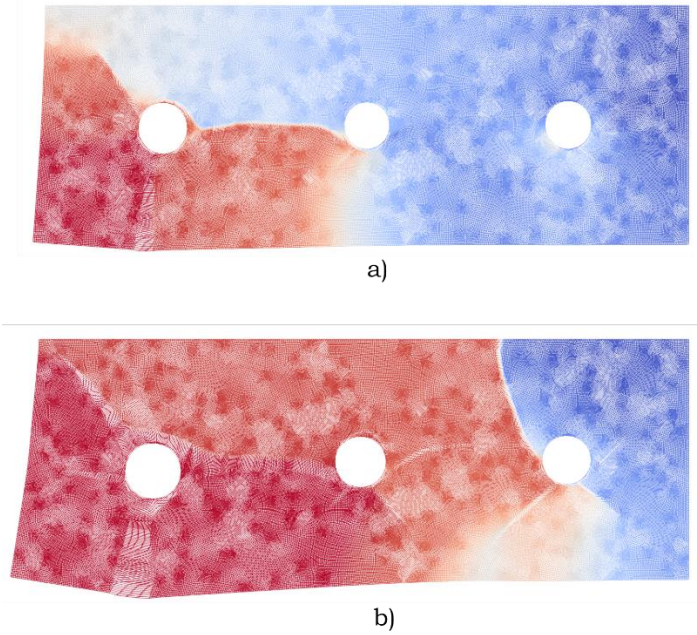

Figure 15 Results for the double side diffusion test with three rebars. Displacement field at different times: a) first internal crack propagation; b) complete spalling of the concrete cover.

5. Conclusions

A predictive computational tool has been developed which permits to investigate the phenomenon of carbonation-induced corrosion cracking. In particular, the proposed model can describe the effects of the carbon dioxide diffusion into the concrete pores and the associated chemical reactions which are responsible for the concrete carbonation process. Changes in the material mechanical properties induced by the carbonation of concrete are also considered. Eventually, as the value of the pH lowers around the rebar, the passive layer dissolves and the corrosion process starts. Using the electrochemical equations, the formation of the rust deposits is evaluated and introduced in the model as a material parameter change of the rebar portion affected by corrosion. Lastly, using the swelling associated with the rust formation as mechanical deformation, the complex fracture pattern which characterize the cover cracking phenomenon is described via the phase field approach.

After the validation of the model against experimental results present in the literature, two different setups have been investigated: single rebar specimen and three rebar specimens. The single rebar test permits to illustrate the capabilities of the model. In fact, as the carbonation front advances within the specimen, rust deposits form around the rebar and cracks propagate toward the edges of the specimen until spalling of the concrete cover is observed. Instead, the three-rebar test focuses on the application of the model on a more realistic RC section where multiple steel rebars influence the cracking phenomenon. While spalling of the cover is also observed at the end of the simulation, the developed model is capable to capture the formation an additional crack which connects the three rebars, causing debonding between the concrete and steel.

At its current state, the model is capable to correctly model the cracking phenomenon of the concrete cover due to the carbonation induced corrosion of the rebar. The interactions between the different phenomena are considered and different setups can be easily investigated. Spalling of the concrete cover is observed at a faster rate compared to a real degradation process as it develops after roughly 8 years. The reason for this faster degradation process is due to the absence of the moisture transport within the concrete which affects the carbon dioxide diffusion as well as the cathodic current by limiting the oxygen supply to the steel rebar surface.

The proposed model should be seen as a first step of a wider project. In fact, future developments will include relative humidity changes and material heterogeneities to simulate more complex and realistic scenarios. Moreover, the adaptive refinement technique proposed in (Freddi & Mingazzi, 2022) will be added to ease the computational requirement of the simulation in order to study larger domains, aiming to apply the proposed method in the analysis and assessment of the condition of existing structures. In parallel, an extensive experimental campaign will be implemented to calibrate material parameters and to improve the results.

References

Ahmad, S. (2003). Reinforcement corrosion in concrete structures, its monitoring and service life prediction - A review. *Cement and Concrete Composites*, *25*(4-5 SPEC), 459–471. https://doi.org/10.1016/S0958-9465(02)00086-0

Alessi, R., Freddi, F., & Mingazzi, L. (2020). Phase-field numerical strategies for deviatoric driven fractures. *Computer Methods in Applied Mechanics and Engineering*, *359*, 112651. https://doi.org/10.1016/j.cma.2019.112651

Alessi, R., Marigo, J.-J. J.-J., & Vidoli, S. (2015). Gradient damage models coupled with plasticity: Variational formulation and main properties. *Mechanics of Materials*, *80*(Part B), 351–367. https://doi.org/10.1016/j.mechmat.2013.12.005

Alessi, R., Marigo, J.-J., & Vidoli, S. (2014). Gradient Damage Models Coupled with Plasticity and Nucleation of Cohesive Cracks. *Archive for Rational Mechanics and Analysis*, *214*(2), 575–615. https://doi.org/10.1007/s00205-014-0763-8

Amor, H., Marigo, J.-J., & Maurini, C. (2009). Regularized formulation of the variational brittle fracture with unilateral contact: Numerical experiments. *Journal of the Mechanics and Physics of Solids*, *57*(8), 1209–1229.

Andrade, C. (2007). Corrosion of steel reinforcement. In *Environmental Deterioration of Materials* (Vol. 28). https://doi.org/10.2495/978-1-84564-032-3/06

Andrade, C., Alonso, C., & Molina, F. J. (1993). Cover cracking as a function of bar corrosion: Part I-Experimental

test. *Materials and Structures*, *26*(8), 453–464. https://doi.org/10.1007/BF02472805
Ansari, T. Q., Xiao, Z., Hu, S., Li, Y., Luo, J.-L., & Shi, S.-Q. (2018). Phase-field model of pitting corrosion kinetics in metallic materials. *Npj Computational Materials*, *4*. https://doi.org/https://doi.org/10.1038/s41524-018-0089-4
Arndt, D., Bangerth, W., Davydov, D., Heister, T., Heltai, L., Kronbichler, M., Maier, M., Pelteret, J. P., Turcksin, B., & Wells, D. (2021). The DEAL.II finite element library: Design, features, and insights. *Computers and Mathematics with Applications*, *81*, 407–422. https://doi.org/10.1016/j.camwa.2020.02.022
Bangerth, W., Hartmann, R., & Kanschat, G. (2007). deal.II - a General Purpose Object Oriented Finite Element Library. *ACM Trans. Math. Softw.*, *33*(4), 24/1--24/27.
Bažant, Z. P. (1979a). *Model for steel corrosion in concrete sea structures - Theory*.
Bažant, Z. P. (1979b). *Model for steel corrosion in concrete sea structures - Applications*.
Bertolini, L., Elsener, B., Pedeferri, P., Redaelli, E., & Polder, R. B. (2013). *Corrosion of Steel in Concrete: Prevention, Diagnosis, Repair, 2nd Edition* (2nd ed.). Wiley-VCH.
Bhargava, K., Ghosh, A. K., Mori, Y., & Ramanujam, S. (2006). Analytical model for time to cover cracking in RC structures due to rebar corrosion. *Nuclear Engineering and Design*, *236*(11), 1123–1139. https://doi.org/10.1016/j.nucengdes.2005.10.011
Bonetti, E., Cavaterra, C., Freddi, F., Grasselli, M., & Natalini, R. (2019). A nonlinear model for marble sulphation including surface rugosity: Theoretical and numerical results. *Communications on Pure and Applied Analysis*, *18*(2), 977–998. https://doi.org/10.3934/cpaa.2019048
Bonetti, E., Cavaterra, C., Freddi, F., Grasselli, M., & Natalini, R. (2021). Chemomechanical Degradation of Monumental Stones: Preliminary Results. In *Mathematical Modeling in Cultural Heritage* (Vol. 41, pp. 59–72). https://doi.org/10.1007/978-3-030-58077-3_4
Borden, M. J., Hughes, T. J. R., Landis, C. M., & Verhoosel, C. V. (2014). A higher-order phase-field model for brittle fracture: Formulation and analysis within the isogeometric analysis framework. *Computer Methods in Applied Mechanics and Engineering*, *273*, 100–118. https://doi.org/http://dx.doi.org/10.1016/j.cma.2014.01.016
Bossio, A., Fabbrocino, F., Monetta, T., Lignola, G. P., Prota, A., Manfredi, G., & Bellucci, F. (2019). Corrosion effects on seismic capacity of reinforced concrete structures. *Corrosion Reviews*, *37*(1), 45–56. https://doi.org/10.1515/corrrev-2018-0044
Bourdin, B., Francfort, G. A., & Marigo, J.-J. (2000). Numerical experiments in revisited brittle fracture. *Journal of the Mechanics and Physics of Solids*, *48*(4), 797–826. https://doi.org/10.1016/S0022-5096(99)00028-9
Bourdin, B., Francfort, G. A., & Marigo, J.-J. (2008). The variational approach to fracture. *J. Elasticity*, *91*(1–3), 5–148. https://doi.org/10.1007/s10659-007-9107-3
Broomfield, J. P. (2003). *Corrosion of steel in concrete*.
Bui, T. Q., & Hu, X. (2021). A review of phase-field models, fundamentals and their applications to composite laminates. *Engineering Fracture Mechanics*, *248*. https://doi.org/10.1016/j.engfracmech.2021.107705
Bullard, J. W., Jennings, H. M., Livingston, R. A., Nonat, A., Scherer, G. W., Schweitzer, J. S., Scrivener, K. L., & Thomas, J. J. (2011). Mechanisms of cement hydration. In *Cement and Concrete Research* (Vol. 41, Issue 12, pp. 1208–1223). https://doi.org/10.1016/j.cemconres.2010.09.011
Choe, G., Shinohara, Y., Kim, G., Lee, S., Lee, E., & Nam, J. (2020). Concrete Corrosion Cracking and Transverse Bar Strain Behavior in a Reinforced Concrete Column under Simulated Marine Conditions. *Applied Science*, *10*. https://doi.org/https://doi.org/10.3390/app10051794
Chukwudozie, C., Bourdin, B., & Yoshioka, K. (2019). A variational phase-field model for hydraulic fracturing in porous media. *Computer Methods in Applied Mechanics and Engineering*, *347*, 957–982. https://doi.org/10.1016/j.cma.2018.12.037
Clarelli, F., De Filippo, B., & Natalini, R. (2014). Mathematical model of copper corrosion. *Applied Mathematical Modelling*, *38*, 4804–4816. https://doi.org/https://doi.org/10.1016/j.apm.2014.03.040
De Jong, M., Chen, W., Angsten, T., Jain, A., Notestine, R., Gamst, A., Sluiter, M., Ande, C. K., Van Der Zwaag, S., Plata, J. J., Toher, C., Curtarolo, S., Ceder, G., Persson, K. A., & Asta, M. (2015). Charting the complete elastic properties of inorganic crystalline compounds. *Scientific Data*, *2*, 1–13. https://doi.org/10.1038/sdata.2015.9
Fang, X., Pan, Z., & Chen, A. (2022). *Phase field modelling of concrete cracking for non-uniform corrosion of rebar*.

Fernandez, I., Herrador, M. F., Marì, A. R., & Bairàn, J. M. (2016). Structural effects of steel reinforcement corrosion on statically indeterminate reinforced concrete members. *Materials and Structures*, *49*, 4959–4973. https://doi.org/https://doi.org/10.1617/s11527-016-0836-2

Freddi, F., & Iurlano, F. (2017). Numerical insight of a variational smeared approach to cohesive fracture. *Journal of the Mechanics and Physics of Solids*, *98*, 156–171. https://doi.org/http://dx.doi.org/10.1016/j.jmps.2016.09.003

Freddi, F., & Mingazzi, L. (2022). Mesh refinement procedures for the phase field approach to brittle fracture. *Computer Methods in Applied Mechanics and Engineering*, *388*, 114214. https://doi.org/10.1016/j.cma.2021.114214

Freddi, F., & Royer-Carfagni, G. (2010). Regularized variational theories of fracture: A unified approach. *Journal of the Mechanics and Physics of Solids*, *58*(8), 1154–1174. https://doi.org/http://dx.doi.org/10.1016/j.jmps.2010.02.010

Freddi, F., & Royer-Carfagni, G. (2011). Variational fracture mechanics to model compressive splitting of masonry-like materials. *Annals of Solid and Structural Mechanics*, *2*(2–4), 57–67. https://doi.org/10.1007/s12356-011-0018-4

Freddi, F., & Royer-Carfagni, G. (2014). Plastic Flow as an Energy Minimization Problem. {N}umerical Experiments. *Journal of Elasticity*, *116*(1), 53–74.

Freddi, F., & Royer-Carfagni, G. (2016). Phase-field slip-line theory of plasticity. *Journal of the Mechanics and Physics of Solids*, *94*, 257–272. https://doi.org/10.1016/j.jmps.2016.04.024

Giavarini, C., Santarelli, M. L., Natalini, R., & Freddi, F. (2008). A non-linear model of sulphation of porous stones: Numerical simulations and preliminary laboratory assessments. *Journal of Cultural Heritage*, *9*(1), 14–22. https://doi.org/10.1016/j.culher.2007.12.001

Hansson, C. M., Poursaee, A., & Laurent, A. (2006). Macrocell and microcell corrosion of steel in ordinary Portland cement and high performance concretes. *Cement and Concrete Research*, *36*(11), 2098–2102. https://doi.org/10.1016/j.cemconres.2006.07.005

Hu, X., Xu, H., Xi, X., Zhang, P., & Yang, S. (2022). Meso-scale phase field modelling of reinforced concrete structures subjected to corrosion of multiple reinforcements. *Construction and Building Materials*, *321*. https://doi.org/10.1016/j.conbuildmat.2022.126376

Huet, B., L'hostis, V., Santarini, G., Feron, D., & Idrissi, H. (2007). Steel corrosion in concrete: Determinist modeling of cathodic reaction as a function of water saturation degree. *Corrosion Science*, *49*(4), 1918–1932. https://doi.org/10.1016/j.corsci.2006.10.005

Hunkeler, F. (1997). Monitoring of repaired reinforced concrete structures by means of resistivity measurements. *Materials Science Forum*, *247*, 93–106. https://doi.org/10.4028/www.scientific.net/msf.247.93

Imperatore, S., & Rinaldi, Z. (2019). Cracking in Reinforced Concrete Structures Damaged by Artificial Corrosion: An Overview. *Open Constr. Build. Technol. J.*, *13*.

Imperatore, S., Rinaldi, Z. Z., & Drago, C. (2017). Degradation relationships for the mechanical properties of corroded steel rebars. *Construction and Building Materials*, *148*. https://doi.org/https://doi.org/10.1016/j.conbuildmat.2017.04.209

Isgor, O. B., & Razaqpur, A. G. (2004). Finite element modeling of coupled heat transfer, moisture transport and carbonation processes in concrete structures. *Cement and Concrete Composites*, *26*(1), 57–73. https://doi.org/10.1016/S0958-9465(02)00125-7

Isgor, O. B., & Razaqpur, A. G. (2006). Modelling steel corrosion in concrete structures. *Materials and Structures/Materiaux et Constructions*, *39*(287), 291–302. https://doi.org/10.1617/s11527-005-9022-7

Johannesson, B. F. (1997). *Nonlinear Transient Phenomena in Porous Media with Special Regard to Concrete and Durability*.

Lancioni, G., & Royer-Carfagni, G. (2009). The Variational Approach to Fracture Mechanics. A Practical Application to the French Panthéon in Paris. *Journal of Elasticity*, *95*(1), 1–30. https://doi.org/10.1007/s10659-009-9189-1

Lin, G., Liu, Y. H., & Xiang, Z. H. (2010). A mathematical model for prediction of time corrosion initiation to corrosion cracking in RC structures. *Materials and Corrosion*, *61*. https://doi.org/https://doi.org/10.1002/maco.200905438

Lin, X., Peng, M., Lei, F., Tan, J., & Shi, H. (2017). Analytical model of cracking due to rebar corrosion expansion in concrete considering the structure internal force. *AIP Advances*, *7*.

https://doi.org/https://doi.org/10.1063/1.5016454
Mai, W., Soghrati, S., & Buchheit, R. G. (2016). A phase field model for simulating the pitting corrosion. *Corrosion Science*, *110*, 157–166. https://doi.org/https://doi.org/10.1016/j.corsci.2016.04.001
Medagoda Arachchige, A. D. (2008). Influence of cement content on corrosion resistance. *Proceedings of Institution of Civil Engineers: Construction Materials*, *161*(1), 31–39. https://doi.org/10.1680/coma.2008.161.1.31
Mesgarnejad, A., Bourdin, B., & Khonsari, M. M. (2015). Validation simulations for the variational approach to fracture. *Computer Methods in Applied Mechanics and Engineering*, *290*, 420–437. https://doi.org/10.1016/j.cma.2014.10.052
Molina, F. J., Alonso, C., & Andrade, C. (1993). Cover cracking as a function of bar corrosion: Part 2 - Numerical model. *Materials and Structures*, *26*, 532–548.
Nguyen, Q. T., Caré, S., Berthaud, Y., Millard, A., & Ragueneau, F. (2011). Experimental and numerical behaviour of reinforced mortar plates subjected to accelerated corrosion. *Int. J. Numer. Anal. Meth. Geomech.*, *35*, 1141–1159. https://doi.org/https://doi.org/10.1002/nag.947
Ou, Y.-C., Susanto, Y. T. T., & Roh, H. (2016). Tensile behavior of naturally and artificially corroded steel bars. *Construction and Building Materials*, *103*. https://doi.org/https://doi.org/10.1016/j.conbuildmat.2015.10.075
Ouglova, A., Berthaud, Y., Foct, F., François, M., & Ragueneau, F. (2008). The influence of corrosion on bond properties between concrete and reinforcement in concrete structures. *Materials and Structures*, *41*, 969–980. https://doi.org/https://doi.org/10.1617/s11527-007-9298-x
Papadakis, V. G., Vayenas, C. G., & Fardis, M. N. (1991a). Fundamental modeling and experimental investigation of concrete carbonation. *ACI Materials Journal*, *88*(4), 363–373. https://doi.org/10.14359/1863
Papadakis, V. G., Vayenas, C. G., & Fardis, M. N. (1991b). Physical and chemical characteristics affecting the durability of concrete. *ACI Materials Journal*, *88*(2), 186–196. https://doi.org/10.14359/1993
Petre-Lazar, I. (2000). *Évaluation du comportement en service des ouvrages en béton armé soumis à la corrosion des aciers: outil d'aide à la décision*.
Pham, K., Amor, H., Marigo, J.-J., & Maurini, C. (2011). Gradient damage models and their use to approximate brittle fracture. *International Journal of Damage Mechanics*, *20*(4), 618–652. https://doi.org/10.1177/1056789510386852
Popov, B. N. (2015). Electrochemical Kinetics of Corrosion. In *Corrosion Engineering*. https://doi.org/10.1016/b978-0-444-62722-3.00003-3
Raupach, M. (1996a). *Investigations on the influence of oxygen on corrosion of steel in concrete-Part 2* (Vol. 29).
Raupach, M. (1996b). *Investigations on the influence of oxygen on corrosion of steel in concrete-Part l* (Vol. 29).
Richard, B., Quiertant, M., Bouteiller, V., Delaplace, A., Adelaide, L., Regueneau, F., & Cremona, C. (2016). Experimental and numerical analysis of corrosion-induced cover cracking in reinforced concrete sample. *Computers and Concrete*, *18*, 421–439. https://doi.org/https://doi.org/10.12989/cac.2016.18.3.421
Richard, B., Regueneau, F., Cremona, C., Adelaide, L., & Tailhan, J. L. (2010). A three-dimensional steel/concrete interface model including corrosion effects. *Engineering Fracture Mechanics*, *77*. https://doi.org/https://doi.org/10.1016/j.engfracmech.2010.01.017
Rodrigues, R., Gaboreau, S., Gance, J., Ignatiadis, I., & Betelu, S. (2021). Reinforced concrete structures: A review of corrosion mechanisms and advances in electrical methods for corrosion monitoring. *Construction and Building Materials*, *269*, 121240. https://doi.org/10.1016/j.conbuildmat.2020.121240
Sheng, J., & Xia, J. (2017). Effect of simulated pitting corrosion on the tensile properties of steel. *Construction and Building Materials*, *131*, 90–100. https://doi.org/https://doi.org/10.1016/j.conbuildmat.2016.11.037
Stefanoni, M., Angst, U., & Elsener, B. (2018). Corrosion rate of carbon steel in carbonated concrete – A critical review. *Cement and Concrete Research*, *103*(June 2017), 35–48. https://doi.org/10.1016/j.cemconres.2017.10.007
Sun, G., Zhang, Y., Tian, Y., Bo, L., Shen, J., & Shi, J. (2020). Investigation of Residual Bearing Capacity of Corroded Reinforced Concrete Short Columns under Impact Load Based on Nondestructive Testing. *Mathematical Problems in Engineering*, *2020*. https://doi.org/https://doi.org/10.1155/2020/1901073
Tanné, E., Li, T., Bourdin, B., Marigo, J.-J., & Maurini, C. (2018). Crack nucleation in variational phase-field models of brittle fracture. *Journal of the Mechanics and Physics of Solids*, *110*(Supplement C), 80–99.
Tuutti, K. (1982). *Corrosion of steel in concrete*.
Verma, S. K., Bhadauria, S. S., & Akhtar, S. (2014). Monitoring Corrosion of Steel Bars in Reinforced Concrete Structures. *The Scientific World Journal*, *2014*. https://doi.org/http://dx.doi.org/10.1155/2014/957904

Wu, J. Y., & Chen, W. X. (2022). On the phase-field modeling of fully coupled chemo-mechanical deterioration and fracture in calcium leached cementitious solids. *International Journal of Solids and Structures*, *238*. https://doi.org/10.1016/j.ijsolstr.2021.111380

Wu, J.-Y., Nguyen, V. P., Nguyen, C. T., Sutula, D., Sinaie, S., & Bordas, S. (2019). Phase-field modelling of fracture. *Adv. Appl. Mech.* https://doi.org/https://doi.org/10.1016/bs.aams.2019.08.001

Wu, T., & de Lorenzis, L. (2016). A phase-field approach to fracture coupled with diffusion. *Computer Methods in Applied Mechanics and Engineering*, *312*, 196–223. https://doi.org/10.1016/j.cma.2016.05.024

Yu, S., & Jin, H. (2020). Modeling of the corrosion-induced crack in concrete contained transverse crack subject to chloride ion penetration. *Construction and Building Materials*, *258*. https://doi.org/10.1016/j.conbuildmat.2020.119645

Zhang, Y., & Su, R. K. L. (2020). Corner cracking model for non-uniform corrosion-caused deterioration of concrete cover. *Construction and Building Materials*, *234*. https://doi.org/https://doi.org/10.1016/j.conbuildmat.2019.117410

Zhuang, X., Zhou, S., Huynh, G. D., Areias, P., & Rabczuk, T. (2022). Phase field modeling and computer implementation: A review. In *Engineering Fracture Mechanics* (Vol. 262). Elsevier Ltd. https://doi.org/10.1016/j.engfracmech.2022.108234